PPARγ deacetylation dissociates thiazolidinedione's metabolic benefits from its adverse effects

Michael J. Kraakman,[1,2] Qiongming Liu,[1,3] Jorge Postigo-Fernandez,[1,4] Ruiping Ji,[5] Ning Kon,[6] Delfina Larrea,[7] Maria Namwanje,[1,3] Lihong Fan,[1,3,8] Michelle Chan,[9] Estela Area-Gomez,[7] Wenxian Fu,[10] Remi J. Creusot,[1,4] and Li Qiang[3]

[1]Naomi Berrie Diabetes Center, [2]Department of Medicine, [3]Department of Pathology and Cell Biology, [4]Department of Medicine, Columbia Center for Translational Immunology, [5]Center for Advanced Cardiac Care, Department of Medicine, Division of Cardiology, [6]Institute for Cancer Genetics and Department of Pathology, and [7]Department of Neurology, College of Physicians and Surgeons, Columbia University New York, New York, USA. [8]Department of Cardiology, The First Affiliated Hospital of Xi'an Jiao Tong University, Xi'an City, Shaanxi Province, China. [9]Department of Biological Sciences, Columbia University, New York, New York, USA. [10]Department of Pediatrics, UCSD, La Jolla, California, USA.

Thiazolidinediones (TZDs) are PPARγ agonists with potent insulin-sensitizing effects. However, their use has been curtailed by substantial adverse effects on weight, bone, heart, and hemodynamic balance. TZDs induce the deacetylation of PPARγ on K268 and K293 to cause the browning of white adipocytes. Here, we show that targeted PPARγ mutations resulting in constitutive deacetylation (K268R/K293R, 2KR) increased energy expenditure and protected from visceral adiposity and diet-induced obesity by augmenting brown remodeling of white adipose tissues. Strikingly, when *2KR* mice were treated with rosiglitazone, they maintained the insulin-sensitizing, glucose-lowering response to TZDs, while displaying little, if any, adverse effects on fat deposition, bone density, fluid retention, and cardiac hypertrophy. Thus, deacetylation appears to fulfill the goal of dissociating the metabolic benefits of PPARγ activation from its adverse effects. Strategies to leverage PPARγ deacetylation may lead to the design of safer, more effective agonists of this nuclear receptor in the treatment of metabolic diseases.

Introduction

The prevalence of metabolic diseases imparts a sense of urgency to research aimed at discovering novel therapeutics for conditions ranging from obesity to diabetes (1). A positive energy balance results in excess lipid deposition in adipocytes, leading to obesity. The latter increases the incidence of type 2 diabetes and its associated comorbidities, including coronary heart disease, stroke, hypertension, nonalcoholic fatty liver disease (NAFLD), cancer, and arthritis (2). The discovery of PPARγ marked a watershed in adipocyte research (3). This nuclear receptor regulates adipocyte differentiation and function, lipid metabolism, inflammation, and other biological processes (4). PPARγ heterodimerizes with retinoid X receptor (RXR) in response to heretofore unidentified ligand(s) and binds to specific DNA sequences to catalyze the formation of transcriptional complexes and regulate gene expression (5). Synthetic PPARγ ligands of the thiazolidinedione (TZD) class, such as rosiglitazone (Rosi) and pioglitazone, are used as insulin sensitizers in the treatment of type 2 diabetes (6, 7) and reduce the incidence of atherosclerotic macrovascular disease in insulin-resistant individuals (8). However, their use has been limited by adverse effects, such as heart failure, fluid retention, weight gain, and fragility fractures (6, 9).

Posttranslational modifications (PTMs), including acetylation (10), phosphorylation (11–13), SUMOylation (14, 15) and O-GlcNAcylation, (16) regulate PPARγ function. Of interest, a 4-day treatment with partial PPARγ agonists that modulate Ser273 phosphorylation improves insulin sensitivity without causing fluid retention in *ob/ob* mice (17). Whether it is possible to separate the effects on insulin sensitization from fluid retention, bone density, and heart function following a longer course is unknown. We have recently discovered that PPARγ is acetylated on multiple lysine residues and that TZDs induce deacetylation of Lys268 and Lys293 in a SirT1-dependent manner. The biological outcome of these modifications is the conversion of energy-storing white adipocytes into brown-like energy-dissipating adipocytes (10). The browning function of PPARγ deacetylation is achieved by selective activation of brown adipocyte genes and repression of white adipocyte genes, without affecting differentiation. We thus proposed that deacetylation of PPARγ modulates its ability to selectively regulate target genes, resulting in metabolic benefits that can be partly ascribed to the browning of white adipose tissue (WAT).

To investigate the metabolic effects of PPARγ deacetylation as well as its potential impact on TZD treatment, we generated mice bearing targeted deacetylation-mimetic mutations of lysine 268 and 293 to arginine (2KR mice). We show that the deacetylated 2KR mutants are protected from obesity and its associated comorbidities through increased energy expenditure as well as from
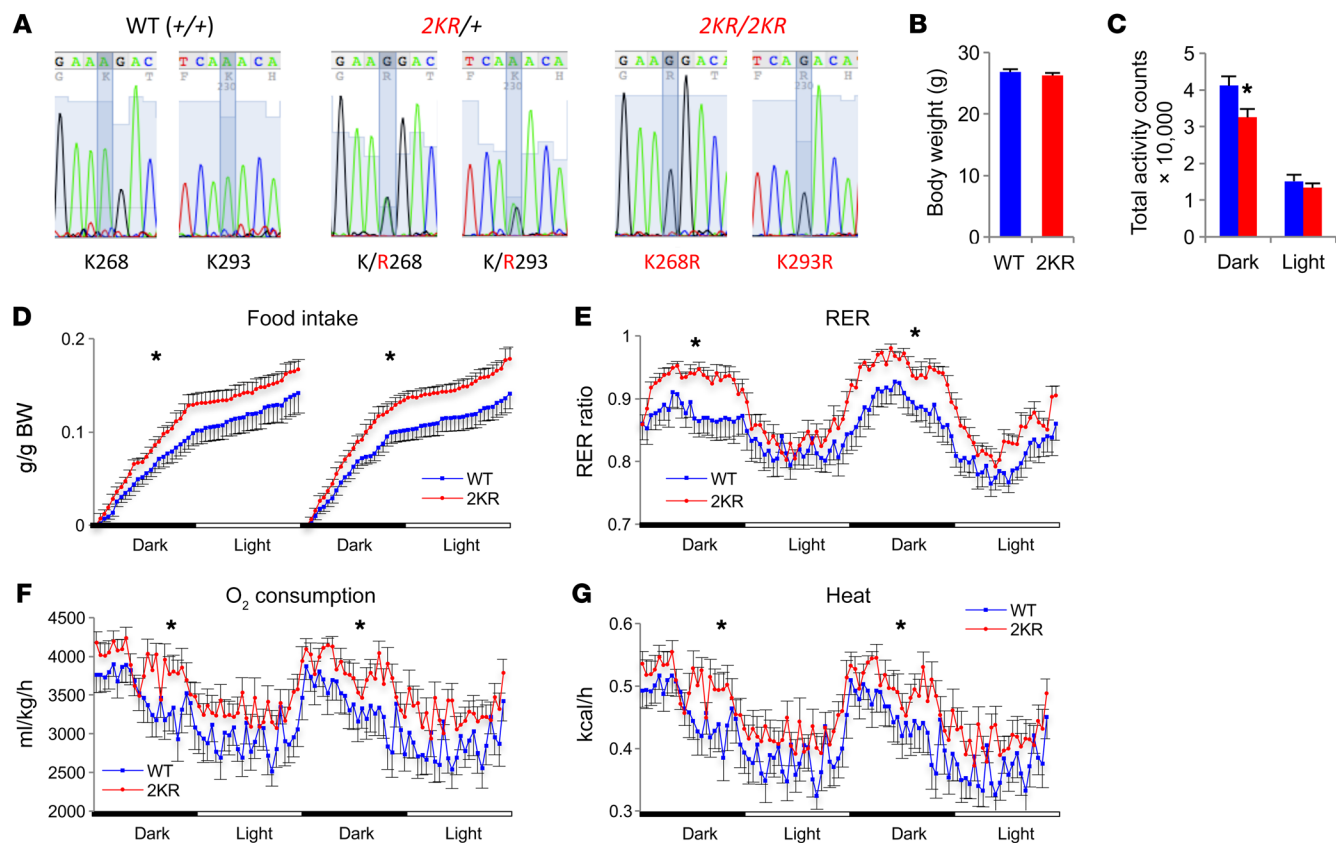
Figure 1. Increased energy wasting in deacetylation-mimetic 2KR mice. (**A**) cDNA sequencing of mRNA from adipose tissue confirmed the replacement of PPARγ WT allele by 2KR mutant allele. The mutated sites were highlighted. (**B**) BW of 4-month-old male mice fed a chow diet. n = 12 WT; n = 12 2KR. (**C–G**) Calorimetric analyses of above mice in **B** at ambient temperature. (**C**) Total activity counts within 1 light/dark cycle. *P < 0.05. (**D**) Food intake on 2 constitutive days. (**E**) RER. (**F**) Oxygen consumption and (**G**) heat production. In **D–G**, *P < 0.05 by t test at multiple detection points. n = 11 WT; n = 12 2KR (1 chamber out of order). Data represent mean ± SEM. Student's t test was used for statistical analyses.

the adverse effects of TZD treatment, such as weight gain, bone loss, and heart lipotoxicity. Our findings indicate that fine-tuning PPARγ's activity through deacetylation can aid in the development of therapeutics for obesity and type 2 diabetes.

Results

PPARγ deacetylation-mimetic 2KR mutations increase energy expenditure. To investigate the physiological effects of PPARγ deacetylation, we generated knockin mice designed to mimic PPARγ deacetylation, PPARγ-K268R/K293R (2KR mice), by replacing exon 5 with a minigene (exons 5–7 and 3′ UTR region) carrying the 2KR mutations (Supplemental Figure 1, A and B; supplemental material available online with this article; https://doi.org/10.1172/JCI98709DS1). cDNA sequencing of the mutant mice confirmed the complete replacement of the WT allele with the *2KR* mutant in homozygous mice (Figure 1A). No altered PPARγ isoform was detected by different exon expression (Supplemental Figure 1C). The 2KR mutant was expressed at a similar level in comparison with the WT PPARγ in inguinal WAT (iWAT), epididymal WAT (eWAT), and brown adipose tissue (BAT) (Supplemental Figure 2, A–D). We used speed congenics to transfer the mutation onto a C57BL/6 background (>97%) (data not shown). 2KR homozygotes were born in Mendelian ratios. As adults, they had body weights (BWs) similar to those of WT controls (Figure 1B) and normal expression of pan-

adipocyte markers (Supplemental Figure 2, B–D). However, when energy homeostasis was assessed by indirect calorimetry, male 2KR mice showed a paradoxical phenotype of decreased activity (Figure 1C and Supplemental Figure 2E) and increased food intake (Figure 1D). The respiratory exchange ratio (RER) in 2KR mice was higher during the dark cycle (Figure 1E), owing to their higher food intake (Figure 1D). Oxygen consumption (Figure 1F) and heat production (Figure 1G) increased, explaining the normal weight despite higher food intake. The phenotype of the male mice was more pronounced than that of the female mice (Supplemental Figure 3). Hereafter, 2KR mice refers to male mice unless specified. Taken together, these data indicate that the 2KR mutant increases energy expenditure independently of altering regular adipose development.

2KR promotes adipose thermogenic activity. Given their increased heat production at ambient temperature, we hypothesized that 2KR mice had enhanced thermogenesis. To test this hypothesis, we exposed mice to the cold. Food intake remained higher in male 2KR mice during a cold challenge (Figure 2A), leading to a higher RER (Figure 2B). Their energy expenditure and heat production remained elevated throughout the cold challenge (Figure 2, C and D), resulting in higher core body temperatures (Supplemental Figure 4, A and B). The increased heat production in 2KR mice could not be accounted for by activity, which returned to normal after cold acclimation (Supplemental Figure
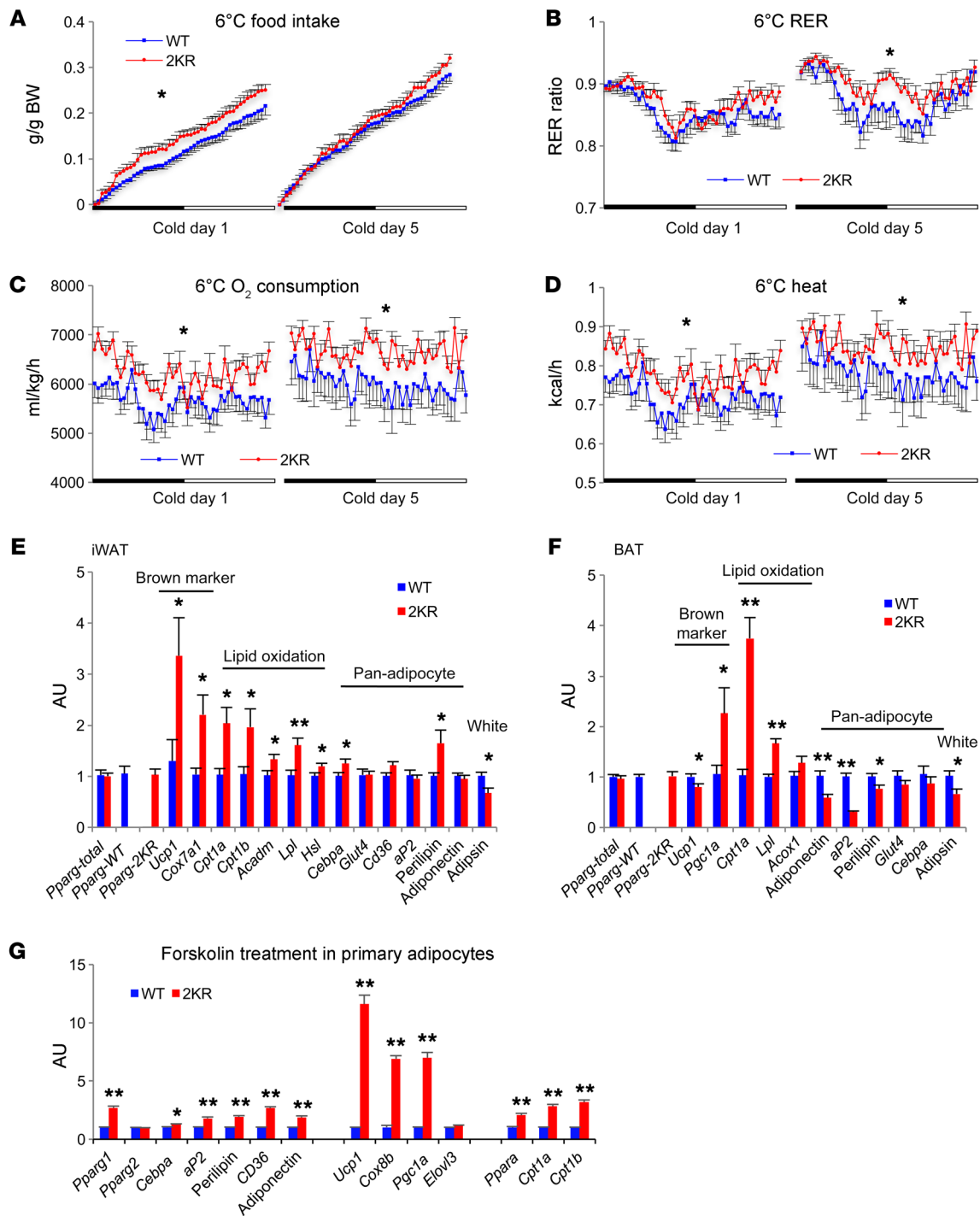
Figure 2. PPARγ deacetylation promotes thermogenic responses. (A–D) Calorimetric analyses of 4-month-old male mice fed a chow diet during acute cold exposure (day 1) and after chronic cold exposure (day 5). (A) Food intake. (B) RER. (C) Oxygen consumption and (D) heat production. *$P < 0.05$ at multiple detection points. $n = 9$ WT; $n = 11$ 2KR (2 WT and 1 mutant mice were hypothermic at the cold exposure and terminated). (E and F) qPCR analyses of gene expression in iWAT (E) and BAT (F) of 5- to 6-month-old chow-fed male mice after 5-day cold exposure. *$P < 0.05$; **$P < 0.01$ for WT vs. 2KR. $n = 6$ WT; $n = 6$ 2KR. (G) qPCR analyses of gene expression in iWAT primary adipocytes after 4-hour forskolin (5 μM) treatment. *$P < 0.05$; **$P < 0.01$ for WT vs. 2KR. $n = 5$ WT; $n = 5$ 2KR. Data represent mean ± SEM. Student's t test was used for statistical analyses.

4C). Changes in insulation were also unlikely, as fur and skin were visually indistinguishable between 2KR and control mice.

We reasoned that nonshivering thermogenesis must be higher in 2KR mice. Brown remodeling of subcutaneous fat contributes to thermogenesis during chronic cold exposure in mice. The 2KR mutant exhibited increased brown adipocyte marker expression in iWAT without an upregulation of *Pgc1a*, *Ppara*, *Cebpb*, and *Prdm16*, suggesting a direct regulation by the 2KR mutant (Figure 2E and Supplemental Figure 4H). Consistently, the expression of key lipid oxidative genes increased, indicating higher levels of fat-
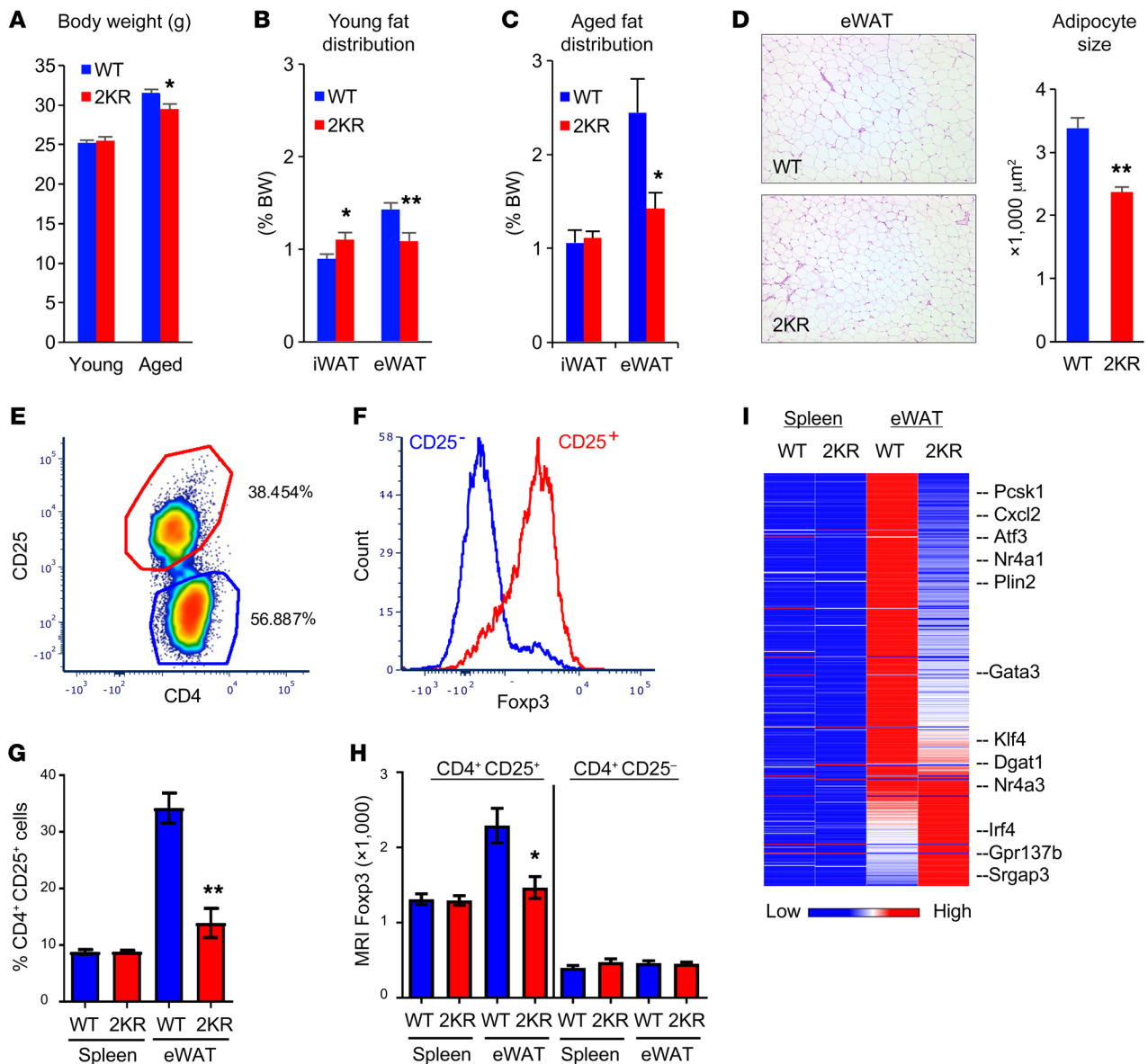
Figure 3. Protection against visceral obesity in 2KR mice. (**A**) BW of chow-fed young (3 months old) and aged (12 to 13 months old) male mice. *$P < 0.05$. n = 8 WT (young); n = 8 2KR (young); n = 9 WT (aged); n = 9 2KR (aged). (**B** and **C**) WAT fat pad sizes in young (**B**) or aged (**C**) male mice sacrificed at ad libitum feeding. *$P < 0.05$; **$P < 0.01$. n = 8 WT (young); n = 8 2KR (young); n = 9 WT (aged); n = 9 2KR (aged). (**D**) Representative H&E staining of visceral epididymal fat (eWAT) and quantification of adipocyte size in aged male mice. Original magnification, ×100. (**E**) Isolation of Tregs (CD4+CD25+) from eWAT of aged male WT mice. (**F**) Confirmation of the presence of fat Treg marker Foxp3 in isolated T cells. (**G**) Proportion of Treg (CD25+) cells among spleen and eWAT CD4+ T cells. **$P < 0.001$. n = 5 WT; n = 5 2KR. This experiment was repeated twice. (**H**) Mean fluorescence intensity (MFI) of Foxp3 in isolated T cells. *$P < 0.05$. n = 5 WT; n = 5 2KR. (**I**) Fat Treg signature gene expression profiling by RNA-seq. Spleen Tregs were used as control. Data represent mean ± SEM. Student's t test was used for statistical analyses.

ty acid oxidation to support iWAT thermogenesis. In BAT, brown genes were largely unaffected except for a 2-fold increase in *Pgc1a* (Figure 2F and Supplemental Figure 4I). *Cpt1a* increased 4-fold, as did *Lpl*, indicating enhanced BAT lipid utilization. PPARγ targets *aP2* and *Perilipin*, which encode lipid droplet–binding proteins and were decreased in BAT, consistent with reduced lipid content (Supplemental Figure 4, D and E). Moreover, most pan-adipocyte markers in iWAT and eWAT were unaffected (Figure 2E and Supplemental Figure 4, F and G), which agreed with our observation that the 2KR mutant selectively regulates brown genes in vitro

(10). The white adipocyte marker *Adipsin* was repressed in iWAT and BAT of 2KR mice (Figure 2, E and F), mimicking an effect associated with TZD-induced browning. Thus, our hypothesis of increased browning by PPARγ deacetylation was borne out in vivo.

The increased energy expenditure in 2KR mice was largely diminished at thermoneutrality (32°C). The mice maintained slightly higher oxygen consumption and heat only during the dark cycle production (Supplemental Figure 5, A and B), likely due to diet-induced thermogenesis that had arisen from their increased food intake during the dark cycle (Supplemental Figure 5C) or from perceived cold
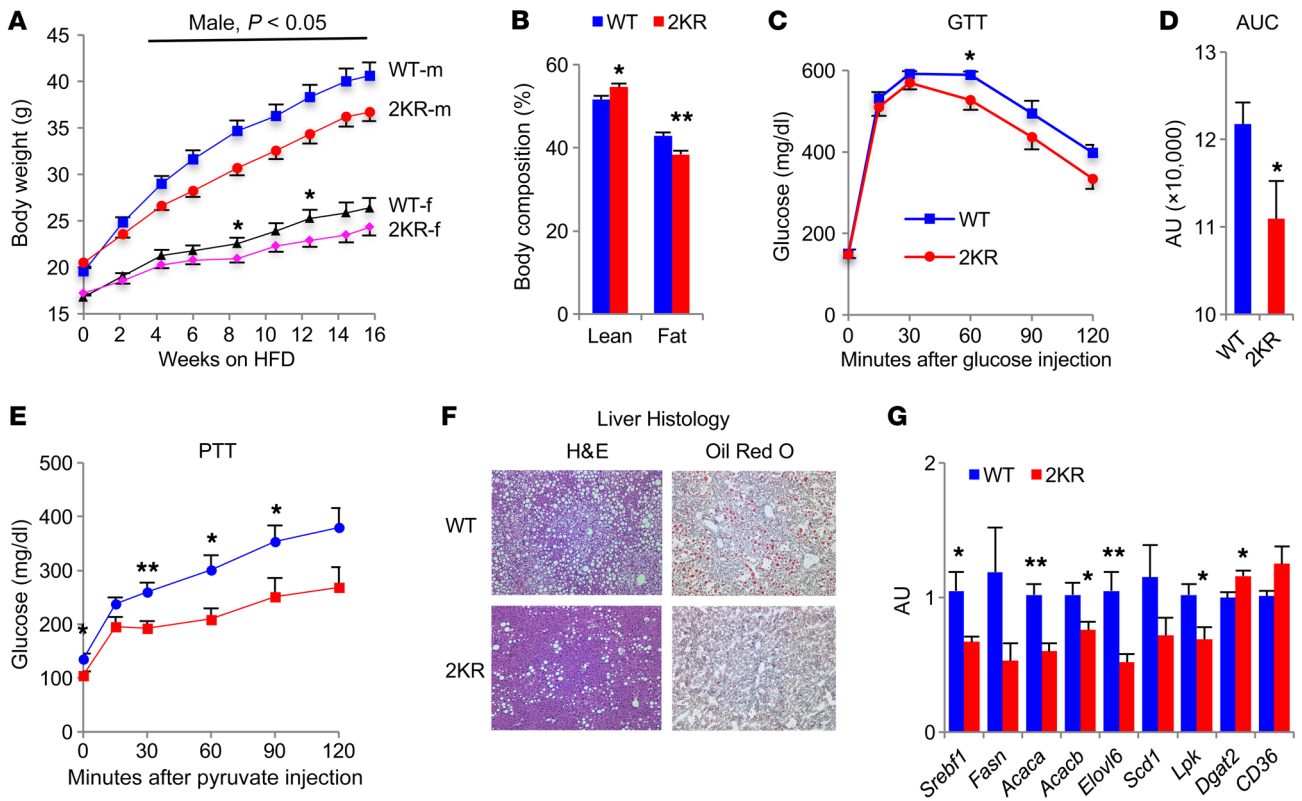
Figure 4. 2KR mice are protected from DIO. (**A**) BW curve of mice that started HFD feeding at 6 weeks old. *$P < 0.05$ for WT vs. 2KR. $n = 16$ male (m) WT; $n = 15$ male 2KR; $n = 14$ female (f) WT; $n = 13$ female 2KR. (**B**) Body composition of male mice after 8 weeks of HFD feeding. *$P < 0.05$; **$P < 0.01$ for WT vs. 2KR. $n = 10$ WT; $n = 9$ 2KR. (**C** and **D**) i.p. GTT (**C**) and AUC (**D**) in male mice at 12 weeks of HFD feeding. *$P < 0.05$ for WT vs. 2KR. $n = 10$ WT; $n = 9$ 2KR. (**E**) PTT in male mice at 12 weeks of HFD feeding. *$P < 0.05$; **$P < 0.01$ for WT vs. 2KR. $n = 10$ WT; $n = 5$ 2KR. (**F** and **G**) Male mice started HFD feeding at 6 weeks old and were sacrificed after 24 weeks on HFD feeding after overnight fasting, followed by 4 to 6 hours of refeeding. (**F**) Improved obesity-associated hepatic steatosis in 2KR mice indicated by histological analysis of the livers by H&E and oil red O staining. Original magnification, ×100. (**G**) qPCR analysis of hepatic lipogenic gene expression. *$P < 0.05$; **$P < 0.01$ for WT vs. 2KR. $n = 7$ WT; $n = 5$ 2KR. Data represent mean ± SEM. Student's *t* test was used for statistical analyses.

stress rather than activity (Supplemental Figure 5D). At thermoneutrality, RER in both WT and 2KR mice was saturated (Supplemental Figure 5E). These data support a catabolic function of PPARγ deacetylation involving increased thermogenesis in adipose tissues.

The browning function of 2KR is adipocyte autonomous. To further establish whether the browning function of PPARγ deacetylation is adipocyte autonomous, we isolated stromal vascular fraction (SVF) cells from iWAT and differentiated them into adipocytes. The 2KR mutation caused a basal increase in the expression of lipid oxidative genes *Ppara* and *Cpt1a* without significantly affecting adipocyte markers and brown genes (Supplemental Figure 6). When the SVF cells were treated with an adipogenic cocktail containing Rosi, 2KR adipocytes showed about 0.5- to 1-fold higher upregulation of adipocyte genes *PPARγ2*, *Adiponectin*, *aP2*, *Cebpa*, and *Perilipin*, while they had a more pronounced induction of genes involved in brown remodeling, including *Ucp1* (8-fold), *Cox8b* (4-fold), and lipid oxidative genes *Ppara* (1-fold), *Cpt1a* (3-fold), and *Cpt1b* (2.5-fold). The white gene *Adipsin* and inflammatory gene *IL-6* were consistently repressed in 2KR adipocytes under both conditions. Moreover, 2KR's regulation of brown genes is target specific, as evidenced by the blunted effects on *Dio2* and *Elovl3* expression. To better mimic the activation of browning in the cold, we treated fully differentiated adipocytes with forskolin. Brown genes *Ucp1*, *Cox8b*, and *Pgc1a* were further upregulated in 2KR

adipocytes, while a much milder effect was observed for regular adipocyte genes (Figure 2G). Again, the lipid oxidative genes *Ppara*, *Cpt1a*, and *Cpt1b* remained upregulated by the 2KR mutant. These data are in full agreement with the browning function of 2KR in vivo and further support the notion that PPARγ deacetylation regulates browning in adipocyte-autonomous and target-specific manners.

2KR mutation inhibits aging-associated visceral obesity and BAT decline. The expression levels of the PPARγ deacetylase SirT1 are lowest in visceral fat, intermediate in iWAT, and highest in BAT (10). Thus, we reasoned that PPARγ acetylation would be affected differently in different fat depots. Despite similar BWs (Figure 3A), 3-month-old 2KR mice had more iWAT and less eWAT than WT mice (Figure 3B). In 12-month-old mice, 2KR mutants had a nearly 10% reduction in BW (Figure 3A), which resulted from a 45% reduction of eWAT, but not iWAT compared with WT mice (Figure 3C). These depot-specific effects of the 2KR mutation were also present in female mice (Supplemental Figure 7). The reduced visceral fat was associated with smaller adipocyte size (Figure 3D). Visceral obesity is associated with insulin resistance and dyslipidemia (18). Along with reduced visceral obesity, aging 2KR mice showed improved glucose tolerance and lower plasma triglycerides (TG) (Supplemental Figure 8, A and B), consistent with a metabolic benefit of the 2KR mutation. The aging-associated BAT dysfunction
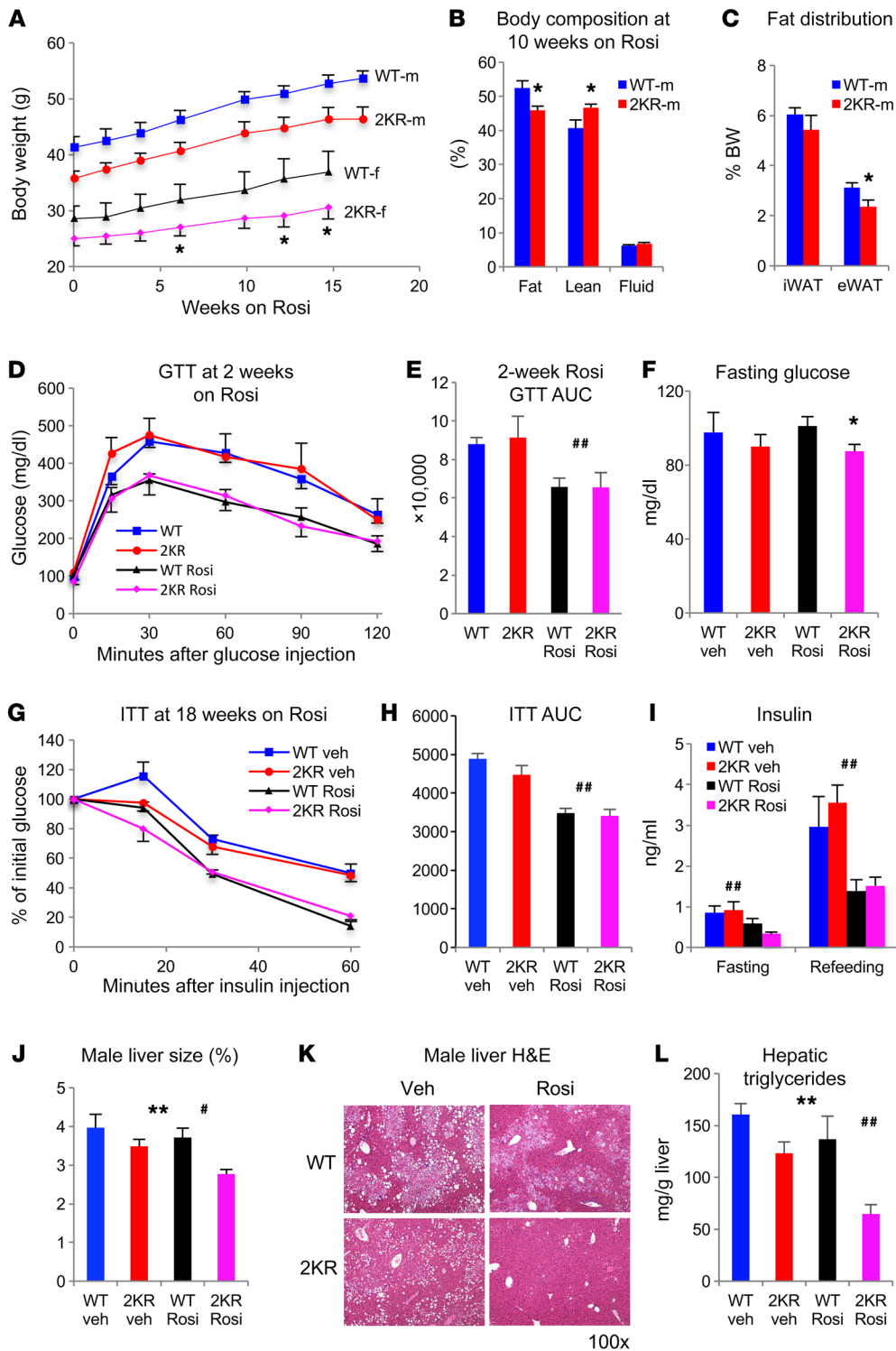
Figure 5. 2KR mice respond to TZD treatment. (A) BW curve on Rosi treatment. Mice were rendered insulin resistant after 16 weeks of HFD feeding (started at 6 weeks old), then switched to a HFD containing Rosi. *$P < 0.05$ for female WT vs. female 2KR by 2-tailed t test. $n = 8$ male WT; $n = 8$ male 2KR; $n = 7$ female WT; $n = 8$ female 2KR. **(B)** Body composition of male mice on Rosi treatment for 10 weeks. Rosi treatment started at 8 weeks of HFD feeding. *$P < 0.05$; **$P < 0.01$ for WT vs. 2KR by 2-tailed t test. $n = 8$ WT; $n = 8$ 2KR. **(C)** WAT fat pad sizes in male mice on 15-week Rosi treatment. Mice were sacrificed after overnight fasting followed by 4 hours of refeeding. *$P < 0.05$ for WT vs. 2KR by 2-tailed t test. $n = 8$ WT; $n = 8$ 2KR. **(D and E)** ipGTT **(D)** and AUC **(E)** before and after 2 weeks of Rosi treatment in BW-matched DIO male mice. $n = 7$ WT; $n = 6$ 2KR. **(F)** Fasting blood glucose levels in male mice after 16 weeks on Rosi treatment. $n = 7$ WT (vehicle [veh]); $n = 7$ 2KR (vehicle); $n = 8$ WT (Rosi); $n = 8$ 2KR (Rosi). **(G and H)** ITT **(G)** and AUC **(H)** in male mice at 18 weeks on Rosi treatment. $n = 7$ WT (vehicle); $n = 7$ 2KR (vehicle); $n = 8$ WT (Rosi); $n = 8$ 2KR (Rosi). **(I)** Plasma insulin levels in male mice after 18 weeks on Rosi treatment. $n = 7$ WT (vehicle); $n = 7$ 2KR (vehicle); $n = 8$ WT (Rosi); $n = 8$ 2KR (Rosi). **(J and L)** Liver size **(J)**, histological analysis by H&E staining **(K)**, and hepatic TG content **(L)** in male mice after 24 weeks of Rosi treatment. Mice were sacrificed after overnight fasting. Original magnification, ×100. $n = 7$ WT (vehicle); $n = 7$ 2KR (vehicle); $n = 8$ WT (Rosi); $n = 8$ 2KR (Rosi). In **D–L**, effects of 2KR (*$P < 0.05$; **$P < 0.01$, WT vs. 2KR) and Rosi (#$P < 0.05$; ##$P < 0.01$, vehicle vs. Rosi) by 2-way ANOVA. In **F–L**, $n = 7$ WT (vehicle); $n = 7$ 2KR (vehicle); $n = 8$ WT (Rosi); $n = 8$ 2KR (Rosi). Data represent mean ± SEM.

was alleviated in 2KR mice, as indicated by their better-preserved expression of thermogenic (*Dio2*, *Cidea*) and lipid oxidative (*Cpt1a*) genes, reduced lipid content, and expression of lipid droplet–associated genes *aP2* and *Perilipin* (Supplemental Figure 8, C and D). iWAT expression of brown genes increased, while expression of white genes *Leptin* and *Adipsin* decreased (Supplemental Figure 8E). These findings demonstrate an antivisceral obesity function of deacetylated PPARγ, in line with its probrowning function.

Next, we questioned whether the metabolic fitness of aging 2KR mice involved Tregs, as inhibition of their accumulation in visceral fat demonstrates similar metabolic improvements during aging (19). We isolated Tregs from the SVF of eWAT in aging animals by FACS of CD4$^+$CD25$^+$ cells (Figure 3E) (19, 20). Treg marker Foxp3 was significantly enriched in sorted CD4$^+$CD25$^+$ cells (Figure 3F), indicating that isolation of fat Tregs was successful (21). The number of Tregs in aging 2KR mice was reduced by nearly 60% compared with that of WT mice
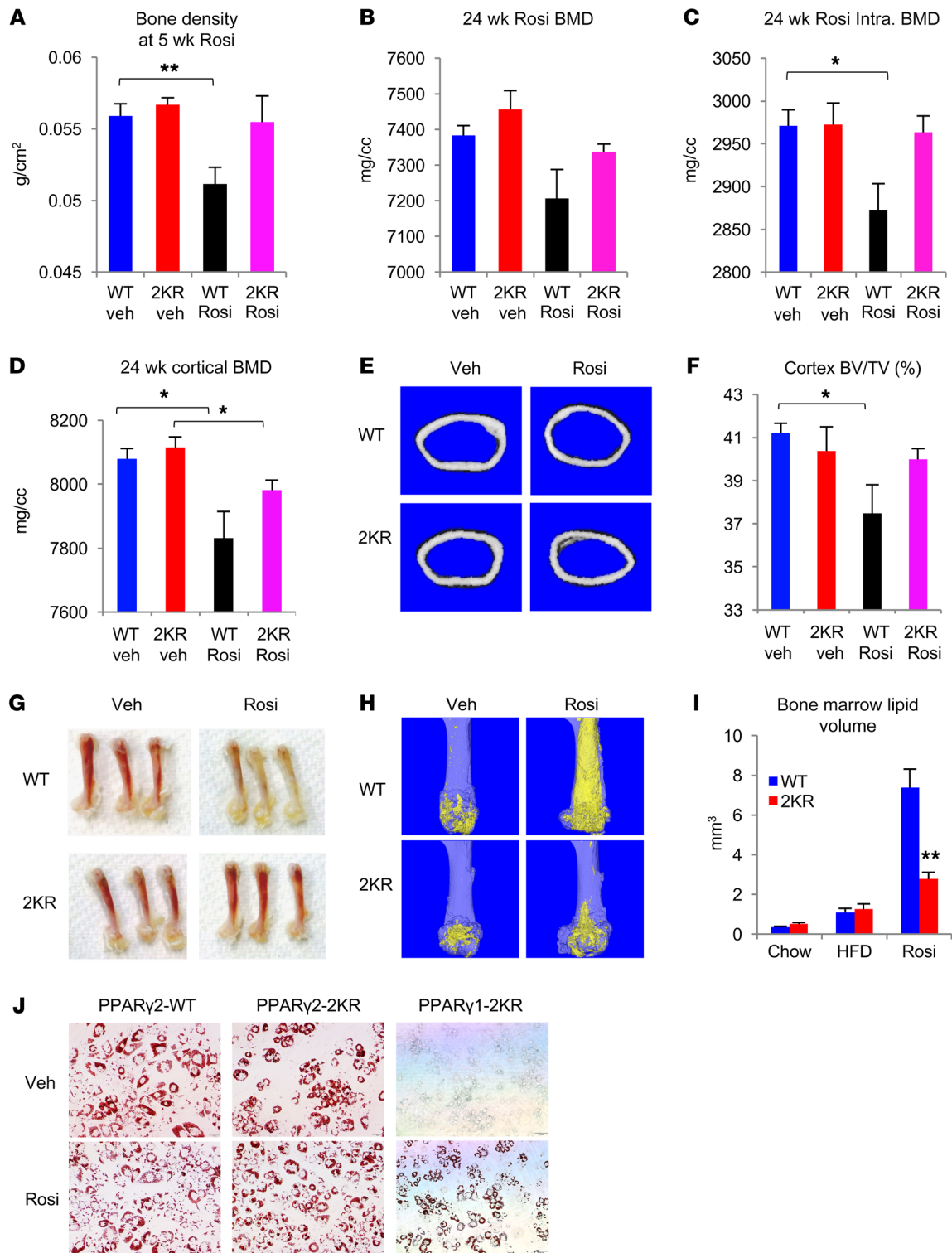
Figure 6. 2KR inhibits TZD-induced bone loss and bone marrow adiposity. (**A**) Bone density determined by DEXA scanning in 12-month-old male mice exposed to HFD for 4 weeks and then treated with Rosi for 5 weeks. **P < 0.01. *n* = 7 WT (vehicle); *n* = 6 2KR (vehicle); *n* = 6 WT (Rosi); *n* = 7 2KR (Rosi). (**B**–**F**) Bone mineral density (**B**), intratrabecular (intra.) bone mineral density (BMD) (**C**), cortical bone mineral density (**D**), representative images of a cross-section of mid-shaft femurs (**E**), and relative cortex volume (**F**) determined by μCT scanning in the femur of male mice on HFD feeding (starting at 6 weeks of age) for 16 weeks, then treated with Rosi for 24 weeks. *P < 0.05. *n* = 7 WT (vehicle); *n* = 7 2KR (vehicle); *n* = 7 WT (Rosi); *n* = 8 2KR (Rosi). (**G**) Gross morphology of femur indicating inhibition of bone marrow adiposity in Rosi-treated 2KR mice. (**H**) Representative osmium tetroxide staining of bone marrow adipocytes assessed by μCT scanning in the femur of male mice after 24 weeks of Rosi treatment. (**I**) Quantification of bone marrow lipid volume in the femurs of male mice by μCT scanning. **P < 0.01. *n* = 12 WT (chow); *n* = 12 2KR (chow); *n* = 7 WT (HFD); *n* = 7 2KR (HFD); *n* = 7 WT (Rosi); *n* = 8 2KR (Rosi). Data represent mean ± SEM. Student's *t* test was used for statistical analyses. (**J**) In *Pparg*⁻/⁻ MEFs, reconstitution of PPARγ2-2KR, but not PPARγ1-2KR, fully rescued adipogenesis as indicated by oil red O staining. Original magnification, ×100.
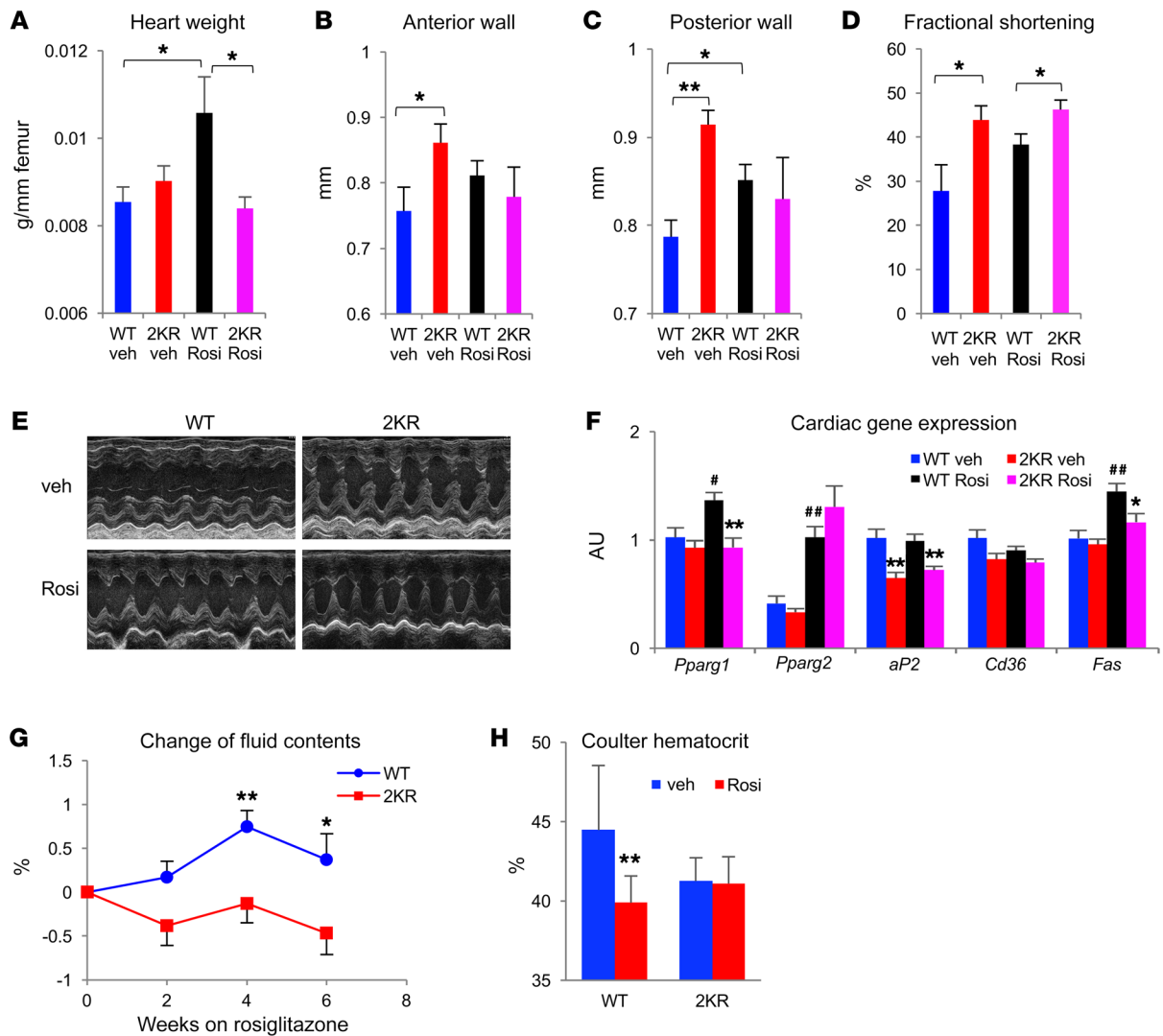
Figure 7. Protection from TZD's cardiovascular side effects in 2KR mice. (**A**–**D**) Heart weight normalized to femur length (**A**), wall thickness (**B** and **C**), and FS (**D**) determined by echocardiography in male mice that were on HFD feeding for 16 weeks, then were treated with Rosi for 24 weeks. *$P < 0.05$; **$P < 0.01$. $n = 7$ WT (vehicle); $n = 7$ 2KR (vehicle); $n = 7$ WT (Rosi); $n = 8$ 2KR (Rosi). (Please note that 1 in WT Rosi group died during echocardiographical measurement). (**E**) Representative M-mode echocardiographic images of left ventricular dimensions. (**F**) qPCR measurement of cardiac lipid-handling gene expression in above male mice. #$P < 0.05$; ##$P < 0.01$ for WT vehicle vs. WT Rosi mice. $n = 6$ WT (vehicle); $n = 6$ 2KR (vehicle); $n = 6$ WT (Rosi); $n = 6$ 2KR (Rosi). *$P < 0.05$; **$P < 0.01$ for WT vs. 2KR mice under the same treatment. $n = 6$ WT (vehicle); $n = 6$ 2KR (vehicle); $n = 6$ WT (Rosi); $n = 6$ 2KR (Rosi). (**G**) Fluid body composition changes in male mice during early treatment of Rosi. Rosi treatment was started at 8 weeks of HFD feeding. *$P < 0.05$; **$P < 0.01$. $n = 8$ WT; $n = 8$ 2KR. (**H**) Hematocrit determined by an automated blood cell counter in male mice after 24 week of Rosi treatment. **$P < 0.01$. $n = 7$ WT (vehicle); $n = 7$ 2KR (vehicle); $n = 7$ WT (Rosi); $n = 8$ 2KR (Rosi). Data represent mean ± SEM. Student's t test was used for statistical analyses.

(Figure 3G), consistent with their reduced eWAT (Figure 3C). Expression of Foxp3 also decreased (Figure 3H). PPARγ is a determining factor of Tregs that reside in visceral fat, but not in other tissues (20). Therefore, we profiled its gene expression by RNA-sequencing (RNA-seq) and found that the fat Treg signature was repressed in 2KR cells (Figure 3I and Supplemental Table 1). In the negative control, spleen Treg accumulation, Foxp3 levels, and gene expression were unaffected by the 2KR mutation (Figure 3, G–I). Together, these data indicate that PPARγ deacetylation inhibits Treg accumulation in visceral fat, possibly contributing to metabolic improvement with aging.

2KR mice are protected from diet-induced obesity. 2KR mice are less energy efficient by virtue of increased browning and energy expenditure. We asked whether deacetylated PPARγ is metaboli-

cally beneficial during chronic nutrient excess. When fed an obesogenic diet (diet-induced obesity [DIO]), 2KR mice gained less weight than controls with lower adiposity (Figure 4, A and B, and Supplemental Figure 9, A–C). 2KR mice had improved glucose tolerance (Figure 4, C and D), likely owing to their lower BW, since this change waned with prolonged high-fat diet (HFD) feeding as their BW difference was diminished (data not shown). Furthermore, their gluconeogenesis was repressed, as demonstrated by improvements in a pyruvate-tolerance test (PTT) (Figure 4E). 2KR mice were also protected from obesity-associated hepatic steatosis (Figure 4F), with decreased expression of key lipogenic genes in liver (Figure 4G). DIO increases lipid deposition in BAT and causes "visceralization" of subcutaneous WAT, a process opposite

of "browning" (22). Both processes were prevented in 2KR mice, as indicated by BAT morphology and increased brown genes *Ucp1*, *Pgc1a*, and *Cox8b* in iWAT (Supplemental Figure 9, D and E). In contrast, white adipocyte marker *Adipsin* and inflammatory factor *Mcp1* decreased in iWAT of 2KR mice without changes to other adipocyte markers. In sum, these data demonstrate that 2KR PPARγ protects against the deleterious metabolic effects of DIO through remodeling of adipose tissue.

2KR mice remain responsive to TZDs. As the effects of the 2KR mutation mimicked those of TZDs, we investigated whether they still responded to treatment with Rosi. To this end, we rendered 2KR and control mice insulin resistant through DIO and then treated them with Rosi (5 mg/kg BW). 2KR mice gained as much weight as WT mice during the treatment (Figure 5A), but their fat accumulation, particularly of eWAT, decreased (Figure 5, B and C). To exclude the confounding effect of BW, we performed a glucose-tolerance test (GTT) in a separate cohort of weight-matched DIO male mice. 2KR mice had the same improvement of glucose tolerance as their weight-matched control mice following Rosi treatment (Figure 5, D and E). However, 2KR mice responded more favorably to Rosi by virtue of lower fasting glucose in both male and female mice (Figure 5F and Supplemental Figure 10A). Furthermore, they showed the same improved insulin tolerance (Figure 5, G and H) and lower insulin levels (Figure 5I) as WT mice, indicating that they responded to TZD at least as much as WT mice. TZD treatment improves hepatic steatosis (23, 24). This benefit was more pronounced in 2KR mice, as indicated by smaller liver size (Figure 5J) and lower lipid content than in control mice (Figure 5, K and L, and Supplemental Figure 10B). Moreover, Rosi-induced BAT lipid accumulation was prevented in 2KR mice (Supplemental Figure 10C). After 24 weeks of Rosi treatment, we also observed a further lowering of plasma cholesterol in 2KR mice, but not of TG (Supplemental Figure 10, D and E). Overall, 2KR mice respond to Rosi with regard to body fat content, glucose homeostasis, hepatic steatosis, and cholesterol.

2KR mice are protected from chronic TZD treatment–induced bone loss. Fragility fractures are a major safety concern associated with TZDs (25). Given the transcriptional selectivity of deacetylated PPARγ, we investigated whether 2KR preempts or curtails TZDs' adverse effects on bone. First, we investigated the short-term effects of Rosi treatment on bone loss using dual energy x-ray absorptiometry (DEXA) following DIO. A 5-week course of Rosi reduced bone density by nearly 10% in WT mice, while this effect was absent in 2KR mice (Figure 6A). We extended the Rosi treatment to 24 weeks to mimic its chronic use in humans and observed a significant 10% bone loss in WT, but a nonsignificant loss in 2KR mice (Figure 6B and Supplemental Figure 11A). Strikingly, the lower intratrabecular mineral density caused by Rosi treatment was completely prevented in 2KR mice (Figure 6C). Rosi treatment also decreased cortical bone mineral density and volume, while 2KR mice were exempted from these deleterious effects (Figure 6, D–F). The bone protection in 2KR mice extended to female mice, even under basal conditions (Supplemental Figure 11B), as well as to aging mice (Supplemental Figure 11C). Taken together, these data demonstrate a bone-protective effect of PPARγ deacetylation.

It has been suggested that TZD-induced bone loss occurs due to enhanced bone marrow adipogenesis at the expense of osteo-

blastogenesis (26, 27). We hypothesized that PPARγ deacetylation blocks TZD-induced bone marrow adipogenesis to improve bone remodeling. Indeed, there was a visible difference. Prolonged Rosi treatment turned the bone marrow yellow in WT mice, but not in 2KR mice (Figure 6G). Histological analyses confirmed the prevention of TZD-induced bone marrow fat accumulation in 2KR femurs (Supplemental Figure 11D). We used osmium tetroxide to stain marrow adipocytes, followed by μCT scanning to quantify bone marrow adiposity in the femur. As expected, Rosi treatment resulted in a marked expansion (of about 7-fold) of bone marrow adipocytes in WT, but not 2KR mice (Figure 6H and Supplemental Figure 11E). Bone marrow osmium tetroxide quantification demonstrated a 60% reduction of fat content in 2KR marrow following Rosi treatment (Figure 6I). Interestingly, unlike the increased bone density in *Pparg*^{+/−} heterozygotes (28), marrow adiposity was not different under basal conditions (chow- or HFD-fed, untreated or vehicle-treated animals) (Figure 6I), suggesting that deacetylation affects target gene selection in response to ligand-dependent activation rather than basal PPARγ function. PPARγ has 2 isoforms, with a broad expression of the shorter isoform PPARγ1 and an adipocyte-restricted longer isoform, PPARγ2. Unlike PPARγ2, PPARγ1 requires TZD to induce adipogenesis (29). We then asked whether deacetylation has different effects on PPARγ isoforms to account for its tissue-specific effects. To this end, we reconstituted PPARγ2-WT, PPARγ2-2KR, and PPARγ1-2KR proteins into *Pparg*^{−/−} MEFs and induced differentiation. PPARγ2-2KR induced adipogenesis, as did PPARγ2-WT. In contrast, PPARγ1-2KR failed to rescue adipogenesis even in the presence of Rosi (Figure 6J).

2KR prevents TZD-dependent myocardial hypertrophy and fluid retention. TZDs have multiple effects on the cardiovascular system, which provides a potential explanation for the increased incidence of heart failure in TZD-treated patients (30). TZD treatment is associated with cardiac hypertrophy in rodents (31, 32). In Rosi-treated WT mice, we did observe increased heart weight, and this effect was absent in 2KR mice (Figure 7A and Supplemental Figure 12A). 2KR mice had thicker anterior and posterior walls than WT mice under basal conditions (Figure 7, B and C), likely owing to the increased workload required to support their higher metabolic rate. In line with this, cardiac function in 2KR mice was improved, as indicated by their increased fractional shortening (FS) and left ventricular systolic dimension (Figure 7, D and E) (33). Upon Rosi treatment, WT and 2KR mice showed comparable heart walls, whereas the latter retained better cardiac function (Figure 7, C–E). Left ventricular end diastolic diameter (LVEDD), a marker of left ventricular structure and function, was unaffected in 2KR mice with or without Rosi treatment (Supplemental Figure 12B). PPARγ activation upregulates hypertrophic genes such as *Acta1*, *ANP*, and *BNP* in the heart, (34, 35), but none of them was affected by the 2KR mutation (Supplemental Figure 12C). In contrast, PPARγ downstream target genes involved in its cardiolipotoxicity, *aP2*, *Cd36*, and *Fas,* were unresponsive to TZDs in the heart of 2KR mice (Figure 7F) (33, 36). TZD treatment also causes edema, which may contribute to congestive heart failure (9). Body fluid content increased upon Rosi treatment in WT mice, but not in 2KR mice (Figure 7G). Hematocrit has been adapted to assess TZD-induced hemodilution (17, 33, 36). Unlike WT mice, 2KR mice showed a blunted response to TZDs on reducing hemo-

dilution (Figure 7H and Supplemental Figure 12D). A subunit of sodium transporter in the renal-collecting duct ENaCγ has been suggested as mediating TZD-caused edema (35, 37, 38), but its activity was not significantly downregulated in 2KR mice (Supplemental Figure 12E). The signs of reduced fluid retention in 2KR mice were not associated with changes in plasma aldosterone levels (Supplemental Figure 12F). Collectively, these data suggest that the cardiovascular effects of Rosi treatment are likely ameliorated in 2KR mice.

Discussion

Uncoupling TZDs' benefits from adverse effects. In this study, we investigated the systemic effects of PPARγ deacetylation in mice homozygous for alleles encoding a deacetylation-mimetic mutant, 2KR. Our key findings include the following: increased energy expenditure due to brown-like features of white adipocytes, resulting in protection from obesity, particularly visceral obesity; and a striking response to Rosi, whereby the drug's metabolic benefits are preserved, while its adverse effects are largely prevented. This work proves that deacetylation-associated PPARγ activation is a theoretically feasible approach toward designing insulin sensitizers devoid of the adverse effects associated with TZDs. PPARγ acetylation is pathophysiologically regulated in response to TZD agonists, SirT1 activation, and other physiological changes (10). It may be possible to combine selective SirT1 activation (39) with TZDs to circumvent undesired effects (40). Partial PPARγ agonists that mimic Ser273 phosphorylation prevent fluid retention during short-term treatment (17). Interestingly, although Lys268/Lys293 acetylation and Ser273 phosphorylation are interdependent (10), the 2KR mutant shows a different gene expression signature in fat Tregs compared with the S273A mutant, suggesting differing modes of action (Supplemental Figure 8F). Our in vivo studies in diet-induced obese and insulin-resistant animals provide proof of principle that targeting PPARγ deacetylation can dissociate the insulin sensitization of TZDs from their adverse side effects. It will be interesting to examine PPARγ acetylation in humans in the context of the pathogenesis and treatment of diabetes and, in particular, to compare adipose tissues to nonadipose tissues. There exists a possibility that diabetic interventions other than TZD treatment may also involve modulations of PPARγ acetylation.

Site(s) of action of PPARγ deacetylation. 2KR mice are energy inefficient; namely, they do not store energy, but seem to dissipate it. Several mechanisms can account for this phenotype. The fact that energy expenditure becomes largely normal in 2KR mice at thermoneutrality, coupled with preservation upon cold exposure, indicates that the thermogenic function of adipose tissue is a major contributor to the mutants' higher energy expenditure. The energy-dissipating effects associated with PPARγ deacetylation consist of 3 aspects: brown remodeling of subcutaneous fat, inhibition of white adipocyte hypertrophy in visceral fat, and preservation of BAT features in response to diet or TZD treatment and aging. These effects likely reflect distinct functions of deacetylation in different fat depots, which are in part dependent on different levels of deacetylase activity (10). In addition, activation of hypothalamic PPARγ increases food intake and decreases activity (41, 42). In this regard, the 2KR mutation mimics TZDs' effects on the central nervous system. However, the increased energy expen-

diture in 2KR mice cannot be attributed to neuronal regulation, since PPARγ in the hypothalamus represses energy expenditure. Another potential site of PPARγ action is the immune system, including eosinophils (43), activated macrophages (44), and visceral fat Tregs (19, 20). From our analysis, it appears that at least visceral fat Tregs are an important site of action of the mutant PPARγ. Nonetheless, further work is required to distinguish the contribution of PPARγ deacetylation from different types of cells from its beneficial metabolic functions.

Why are 2KR mice protected from TZDs' adverse effects on body composition, bone loss, cardiac dysfunction, and fluid retention? In light of the cellular specificity of the effects of 2KR, we speculate that the protective effects of this mutation reflect cellular rather than systemic actions of the mutated PPARγ. The maintenance of bone mass by PPARγ deacetylation can result from a preservation of the physiological balance of differentiation of bone marrow progenitors into osteoblasts and adipocytes, with a contribution from inhibition of bone resorption (45). The cardiac protection in 2KR mice can be mediated by increased lipid utilization and repressed lipid storage — similar to what was observed in fat — leading to reduced lipotoxicity (33). The effects of fluid and electrolyte balance may reflect a specific role of PPARγ deacetylation in the kidney, but it is unlikely that this is through the repression of sodium transporter protein ENaCγ. Intriguingly, in nonadipose tissues, such as heart and kidney, and very likely in the bone, the canonical PPARγ targets are repressed (Figure 7F and Supplemental Figure 12E). Why does the same deacetylation display different effects on PPARγ between adipocytes and other types of cells? A possible explanation is the difference in PPARγ isoform expression: the short PPARγ1 isoform is broadly expressed in nonadipose tissues, while the long isoform PPARγ2 containing an additional 30 amino acids on the N terminus is restricted to adipocytes. Indeed, these 2 lysines localize to the "omega loop" in the ligand-binding domain (LBD) facing the DNA-binding domain (DBD), while the active cofactor binding region helix 12 in LBD localizes to the opposite position, raising the possibility that deacetylation may have distinct effects on these 2 isoforms. Nonetheless, conditional knockins will be necessary to address these questions and investigate the tissue-specific mechanisms of PPARγ deacetylation.

Transcriptional selectivity of PPARγ deacetylation. The resistance to obesity in 2KR mice is reminiscent of *Pparγ* haploinsufficiency (*Pparg*^{+/−}) (46–49) as well as that in mice bearing the Pro12Ala variant (50). However, its mechanism differs. Unlike in these 2 models, the 2KR mutation does not inhibit *aP2*, *Cd36,* and other pan-adipocyte genes in adipocytes, but has a strong effect on stress-response genes *Ucp1* and *Adipsin* and on lipid oxidative genes, such as *Cpt1a*. The selective activation of PPARγ targets seems key to the uncoupling of TZD-dependent insulin sensitization from its undesired side effects. From a mechanistic perspective, how does PPARγ deacetylation achieve transcriptional selectivity? Deacetylated PPARγ preferentially interacts with PRDM16 and disrupts the binding of the transcriptional corepressor NCoR (10). Therefore, it may determine cofactor exchanges in the PPARγ transcriptional complex on acetylation-responsive target promoters, while it may not be required for pan-adipocyte target genes. A parallel mechanism of action of the mutant PPARγ is a change

in DNA-binding affinity. Although Lys268 and Lys293 localize to the LBD of PPARγ, their acetylation may affect cofactors interacting with the DBD. In addition, there are likely tissue- and cell-specific factors that determine the outcome of these transcriptional complexes. Our findings support a body of evidence that PTMs of PPARγ integrate nutrient availability, environmental stimuli, and ligand availability to fine-tune PPARγ's transcriptional activity and regulate its pleiotropic functions.

PPARγ appears to have evolved as a thrifty gene that promotes energy storage during food deprivation, but contributes to obesity and associated disorders when nutrients abound. Seen from such an evolutionary perspective, deacetylation is a mechanism to dampen these features of PPARγ. In a biomedical context, separating the insulin-sensitizing functions of PPARγ from its inimical effects remains a crucial challenge. The findings of this study provide a model to approach this challenge as well as a tool to dissect the complex biology of this critical transcription factor.

Methods

Generation of PPARγ deacetylation-mimetic 2KR mice. The approach is outlined in Supplemental Figure 1A. Properly targeted G418-resistant clones were identified by Southern blotting and confirmed by genomic DNA sequencing. Two independent positive embryonic stem (ES) cell clones were injected into 129/B6 hybrid blastocysts to achieve germline transmission of the *Pparg^{2KR}* allele. Fifteen out of seventeen chimeras from both clones were validated as positive by genotyping and Southern blot. Heterozygous F1 mice with germline transmission were identified by genotyping and genomic DNA sequencing and then bred with *Rosa26-Cre* transgenic mice to delete the LoxP-flanked neomycin resistance gene (*neo*) from the targeted allele. The heterozygous 2KR mice were bred onto a C57BL/6 background (>97%) by using speed congenics (DartMouse).

Animal studies. Mice were housed at $23 \pm 1°C$ on a 12-hour light/12-hour dark cycle with access to food and water ad libitum. The HFD contained 60% calories from fat, 20% from protein, and 20% from carbohydrates and was purchased from Research Diets (D12492). Animals were placed at 6°C (male) or 12°C (female) for 16 hours for acute cold exposure, or 4 to 7 days for chronic cold exposure on a 12-hour light/12-hour dark cycle. Rosi maleate (Avandia) (Abcam, ab142461) was mixed into HFD at 100 mg/kg (Research Diets) to achieve a dose of approximately 5 mg/kg BW. For i.p. GTT and PTT, mice were fasted overnight in fresh bedding cages and i.p. injected with glucose (2 g/kg BW) or pyruvate (1 g/kg BW), respectively. Blood glucose was measured with a Breeze2 glucometer (Bayer) at indicated time points. For the insulin tolerance test (ITT), mice were fasted for 4 hours and injected i.p with insulin (0.75 U insulin/kg BW). Body compositions were determined by nuclear magnetic resonance (NMR) (Bruker Optics). To measure body temperature, animals were anesthetized with isoflurane and implanted with IPTT-300 transponders (Bio Medic Data Systems) subcutaneously. After 4 days of recovery, their body temperature was read by the DAS-7006/7s wireless scanner system (Bio Medic Data Systems). For calorimetric studies, we used the Comprehensive Lab Animal Monitoring System (CLAMS) (Columbus Instruments) with temperature-controlled settings. The whole-body bone density was determined by the Lunar PIXImus2 Densitometer (GE Medical Systems) upon sacrifice. We extracted lipids for the liver to assess hepatic steatosis as previously described (51). Serum metab-

olites were measured with Infinity Triglyceride Reagent (Thermo Scientific), NEFA-HR (2), and total cholesterol (Wako Diagnostics), Mouse Insulin ELISA (MilliporeSigma), and the aldosterone ELISA kit (Abcam, ab136933). Antibodies used for Western blot analysis were as follows: anti-PPARγ (Cell Signaling Technology, catalog 2443), anti-adiponectin (Affinity BioReagents, catalog PA1-054), anti-aP2 (Cell Signaling Technology, catalog 2120), anti-GAPDH (Santa Cruz Biotechnology Inc., catalog sc-25778), anti-perilipin (Cell Signaling Technology, catalog 9349), anti-tubulin (Santa Cruz Biotechnology Inc., catalog sc-58666), anti-actin (Cell Signaling Technology, catalog 8457), and anti-Ucp1 (Abcam, catalog 10983).

SVF isolation. Inguinal fat pads with the lymph nodes removed were dissected from 5- to 6-week-old WT or 2KR mice, followed by mincing and digesting in Liberase TM (Sigma-Aldrich, catalog 5401127001) at 37°C for 20 minutes with gentle agitation. After passing through a 100 μm pore cell strainer, SVF was pelleted by centrifuging at 400 *g* for 5 minutes at 4°C. The pellet was resuspended and plated in basic medium (DMEM supplemented with 10% FBS, 0.5× Pen Strep, 1× gentamycin, 10 mM HEPES, 25 μg/ml sodium ascorbate). Upon reaching 70%–80% confluence, SVF cells were passaged and plated in 6-well plates for experiments. The cells underwent adipogenesis with a standard adipogenic cocktail in the absence or presence of 5 μM Rosi and were harvested on day 7 for analysis. To examine brown gene induction, mature adipocytes were treated with forskolin (5 μM) for 4 hours before harvesting.

Cell cultures. The cDNAs of PPARγ variants, including PPARγ2-WT, PPARγ2-2KR, and PPARγ1-2KR, were cloned into a doxycycline-inducible lentiviral plasmid, pTRIPZ (Thermo Open Biosystems) (29), by using the Quick-Fusion Cloning Kit (Biotool) and were stably overexpressed into *Pparg^{-/-}* mouse embryonic fibroblasts (MEFs) (52) with a selection of puromycin (2.5 μg/ml). Cells were grown in high-glucose DMEM (Corning, 10-017) supplemented with 10% FBS (heat inactivated; Corning, 35-011-CV) and 1× penicillin/streptomycin (Thermo Fisher). Two days prior to adipogenesis, cells were treated with 1 μg/ml doxycycline to induce PPARγ expression. The adipogenic cocktail contained 1 μM dexamethasone, 0.5 mM 3-isobutyl-1-methylxanthine, and 10 μg/ml insulin in the presence or absence of 5 μM Rosi. Two days after induction, cells were maintained into medium containing 2.5 μg/ml insulin and 1 μg/ml doxycycline with or without 5 μM Rosi until fully differentiated. The lipid contents were accessed by oil red O staining.

RNA analysis. Tissues or cells were lysed into TRIzol reagent (Thermo Fisher). After phase separation through the addition of chloroform, RNA was isolated using the NucleoSpin RNA Kit with DNase I digestion (Macherey-Nagel, Thermo Fisher Scientific). To isolate a small amount of RNA from Tregs, the RNeasy Micro Kit (QIAGEN) was used instead. cDNA was synthesized from 1 μg total RNA by using the High-Capacity cDNA Reverse Transcription Kit (Applied Biosystems). Quantitative real-time PCR (qPCR) was performed on a Bio-Rad CFX96 Real-Time PCR system by using the GoTaq qPCR Master Mix (Promega). Relative gene expression levels were calculated using the ΔΔCt method with *TBP* or Cyclophilin A as the reference genes. RNA-seq was conducted at the Columbia Genome Center on an Illumina HiSeq2000 platform. All original microarray data were deposited in the NCBI's Gene Expression Omnibus database (GEO GSE111833). For RNA-seq analysis, a gene expression signature composed of 400 genes that are preferentially overrepresented in fat Tregs was extracted from a published study (using 2-fold cutoff between vis-

ceral fat Treg and spleen Treg) (53). The expression pattern of these fat Treg signature genes was plotted for the RNA-seq data sets of the spleen and fat Tregs from both WT and 2KR mice. The GENE-E module from Broad Institute (https://software.broadinstitute.org/GENE-E/index.html) was used to cluster the expression of fat Treg signature genes among the samples.

Bone processing and analyses. Femurs were excised carefully and cleaned of muscle and connective tissue before fixation in 10% neutral buffered formalin overnight at 4°C. One femur was used for bone microarchitecture analysis and lipid quantification, and the other was decalcified for histology. μCT scanning on a Quantum FX μCT Scanner (PerkinElmer) was employed to assess bone microarchitecture and lipid content. Scans had an energy of 90 kV (55 kV for lipid determination) with a current of 160 μA and a 10 mm field of view (isometric voxel size, 20 μm). For lipid determination, femurs were decalcified for at least 14 days in a 14% EDTA solution changed regularly. Femurs were stained for 48 hours in a 1% osmium tetroxide, 2.5% potassium dichromate solution at room temperature and then washed in tap water for at least 2 hours before being imaged by μCT. Lipid volume was quantified by establishing an arbitrary density threshold, which was applied uniformly to all samples and expressed as mm³ volume within a 350-slice distance from the base of the condyle. Bone mineral densities and lipid volume were quantified with a computer program (Analyse 12.0). H&E staining was performed on decalcified bone sections of 4 μm thickness and imaged using a standard microscope (Nikon ECLIPSE, E400).

Isolation of Tregs from visceral fat. Visceral fat was minced in PBS containing 5 mM EDTA and 0.2% (wt/vol) BSA, then centrifuged at 500 *g* for 5 minutes to remove erythrocytes and free leukocytes. The floating tissue was digested in Digestion solution (0.14 units/ml Liberase TM [Roche Applied Science], 20 mg/ml BSA, 50 U/ml DNase I [Sigma-Aldrich] in DMEM) for 30 minutes at 37°C with agitation. After passing through a 100 μm nylon strainer, the digested tissue was centrifuged at 500 *g* for 5 minutes at 4°C. The pellet was resuspended into red blood lysis buffer and incubated at room temperature for 1 minute, then centrifuged at 500 *g* for 5 minutes at 4°C to deplete erythrocytes. The remaining stromal vascular cells (SVC) were used for Treg isolation and analysis.

The control spleen T cells were enriched first by using the Mouse CD4+ T cell Isolation Kit (STEMCELL Technologies, 19852A) after homogenization. Fat SVC and spleen T cell suspensions were stained with FITC anti-mouse CD4 (100406, BioLegend), APC anti-mouse CD25 (102012, BioLegend), and propidium iodide as a viability dye. Cells were sorted on a BD Influx Cell Sorter at the Columbia Center for Translational Immunology. CD4+CD25+ and CD4+CD25− cells were directly sorted into 0.5 ml TRI Reagent LS (T3934, Sigma-Aldrich), frozen in dry ice, and stored at −80°C for further RNA analysis. We performed extracellular staining of 0.5×10^6 cells for Treg analysis by using anti-mouse CD4-APCCy7 (100414, BioLegend), anti-mouse CD25-APC (102012, BioLegend), anti-mouse CD8-FITC (100706, BioLegend), anti-mouse B220–Pacific Blue (103227, BioLegend), and Zombie Aqua Fixable Viability Dye (77143, BioLegend). The cells were fixed and permeabilized using the True-Nuclear Transcription Factor Buffer Set (424401, BioLegend). We performed the intracellular staining of Foxp3 with anti-mouse/rat Foxp3-PE/APC (12-5773-82, eBioscience). Cells were sorted on the BD Influx cell analyzer at the Columbia Center for Translational Immunology.

Echocardiography. Mice were anesthetized by isoflurane inhalation. Anesthesia was induced by 1.5%–2% isoflurane, reduced to 0.5%–1% once the mouse was asleep. Oxygen gas was flowing at 2 ml/min. The chest skin of the mouse was shaved using a hair remover, and the heart function was evaluated with a 30 MHz high-frequency ultrasound transducer (Visualsonics, VEVO 2100). 2D image and M mode were studied in the parasternal short-axis view at the level of the papillary muscles. Echocardiographic images were analyzed by a researcher blinded to the treatments and genotypes. LVEDD and left ventricular end systolic dimension (LVESD) were measured, and FS was calculated as follows: FS% = [(LVEDD − LVESD)/LVEDD] ×100%.

Hematocrit determinations. Blood was collected from the jugular vein into heparinized capillary tubes about three-quarters full. The filled capillary tubes were sealed on 1 end and centrifuged on the microhematocrit centrifuge for 5 minutes. The results were read by using the micro-hematocrit reading device. Alternatively, hematocrit was also determined in freshly collected mouse blood (via cardiac puncture) using an automated hematological cell counter (Oxford Science Inc.).

Statistics. We used unpaired 2-tailed Student's *t* test and 2-way ANOVA to evaluate statistical significance. $P < 0.05$ was considered a statistically significant change. The data are presented as mean ± SEM.

Study approval. The present studies in animals were reviewed and approved by the Columbia University Animal Care and Utilization Committee.

Author contributions

Acknowledgments

Address correspondence to: Li Qiang, 1150 St. Nicholas Avenue, Room 607A, New York, New York, 10032, USA. Phone: 212.851.4929; Email: lq2123@cumc.columbia.edu.

1. F as in Fat: How Obesity Threatens America's Future 2012. Trust for America's Health. http://healthyamericans.org/report/100/. Accessed April 11, 2018.

2. Guh DP, Zhang W, Bansback N, Amarsi Z, Birmingham CL, Anis AH. The incidence of co-morbidities related to obesity and overweight: a systematic review and meta-analysis. *BMC Public Health*. 2009;9:88.

3. Tontonoz P, Spiegelman BM. Fat and beyond: the diverse biology of PPARgamma. *Annu Rev Biochem*. 2008;77:289–312.

4. Ahmadian M, et al. PPARγ signaling and metabolism: the good, the bad and the future. *Nat Med*. 2013;19(5):557–566.

5. Tontonoz P, et al. Adipocyte-specific transcription factor ARF6 is a heterodimeric complex of two nuclear hormone receptors, PPAR gamma and RXR alpha. *Nucleic Acids Res*. 1994;22(25):5628–5634.

6. Abbas A, Blandon J, Rude J, Elfar A, Mukherjee D. PPAR-γ agonist in treatment of diabetes: cardiovascular safety considerations. *Cardiovasc Hematol Agents Med Chem*. 2012;10(2):124–134.

7. Lehrke M, Lazar MA. The many faces of PPARgamma. *Cell*. 2005;123(6):993–999.

8. Kernan WN, et al. Pioglitazone after Ischemic Stroke or Transient Ischemic Attack. *N Engl J Med*. 2016;374(14):1321–1331.

9. Soccio RE, Chen ER, Lazar MA. Thiazolidinediones and the promise of insulin sensitization in type 2 diabetes. *Cell Metab*. 2014;20(4):573–591.

10. Qiang L, et al. Brown remodeling of white adipose tissue by SirT1-dependent deacetylation of Pparγ. *Cell*. 2012;150(3):620–632.

11. Hu E, Kim JB, Sarraf P, Spiegelman BM. Inhibition of adipogenesis through MAP kinase-mediated phosphorylation of PPARgamma. *Science*. 1996;274(5295):2100–2103.

12. Iankova I, et al. Peroxisome proliferator-activated receptor gamma recruits the positive transcription elongation factor b complex to activate transcription and promote adipogenesis. *Mol Endocrinol*. 2006;20(7):1494–1505.

13. Choi JH, et al. Anti-diabetic drugs inhibit obesity-linked phosphorylation of PPARgamma by Cdk5. *Nature*. 2010;466(7305):451–456.

14. Dutchak PA, et al. Fibroblast growth factor-21 regulates PPARγ activity and the antidiabetic actions of thiazolidinediones. *Cell*. 2012;148(3):556–567.

15. Pascual G, et al. A SUMOylation-dependent pathway mediates transrepression of inflammatory response genes by PPAR-gamma. *Nature*. 2005;437(7059):759–763.

16. Ji S, Park SY, Roth J, Kim HS, Cho JW. O-GlcNAc modification of PPARγ reduces its transcriptional activity. *Biochem Biophys Res Commun*. 2012;417(4):1158–1163.

17. Choi JH, et al. Antidiabetic actions of a non-agonist PPARγ ligand blocking Cdk5-mediated phosphorylation. *Nature*. 2011;477(7365):477–481.

18. Gabriely I, et al. Removal of visceral fat prevents insulin resistance and glucose intolerance of aging: an adipokine-mediated process? *Diabetes*. 2002;51(10):2951–2958.

19. Bapat SP, et al. Depletion of fat-resident Treg cells prevents age-associated insulin resistance. *Nature*. 2015;528(7580):137–141.

20. Cipolletta D, et al. PPAR-γ is a major driver of the accumulation and phenotype of adipose tissue Treg cells. *Nature*. 2012;486(7404):549–553.

21. Weisberg SP, McCann D, Desai M, Rosenbaum M, Leibel RL, Ferrante AW. Obesity is associated with macrophage accumulation in adipose tissue. *J Clin Invest*. 2003;112(12):1796–1808.

22. Cohen P, et al. Ablation of PRDM16 and beige adipose causes metabolic dysfunction and a subcutaneous to visceral fat switch. *Cell*. 2014;156(1-2):304–316.

23. Way JM, et al. Comprehensive messenger ribonucleic acid profiling reveals that peroxisome proliferator-activated receptor gamma activation has coordinate effects on gene expression in multiple insulin-sensitive tissues. *Endocrinology*. 2001;142(3):1269–1277.

24. Nagashima K, et al. Effects of the PPARgamma agonist pioglitazone on lipoprotein metabolism in patients with type 2 diabetes mellitus. *J Clin Invest*. 2005;115(5):1323–1332.

25. Kahn SE, et al. Glycemic durability of rosiglitazone, metformin, or glyburide monotherapy. *N Engl J Med*. 2006;355(23):2427–2443.

26. Rosen ED, et al. PPAR gamma is required for the differentiation of adipose tissue in vivo and in vitro. *Mol Cell*. 1999;4(4):611–617.

27. Wei W, Wan Y. Thiazolidinediones on PPARγ: The Roles in Bone Remodeling. *PPAR Res*. 2011;2011:867180.

28. Akune T, et al. PPARgamma insufficiency enhances osteogenesis through osteoblast formation from bone marrow progenitors. *J Clin Invest*. 2004;113(6):846–855.

29. Li D, et al. Distinct functions of PPARγ isoforms in regulating adipocyte plasticity. *Biochem Biophys Res Commun*. 2016;481(1-2):132–138.

30. Ferrannini E, DeFronzo RA. Impact of glucose-lowering drugs on cardiovascular disease in type 2 diabetes. *Eur Heart J*. 2015;36(34):2288–2296.

31. Duan SZ, Ivashchenko CY, Russell MW, Milstone DS, Mortensen RM. Cardiomyocyte-specific knockout and agonist of peroxisome proliferator-activated receptor-gamma both induce cardiac hypertrophy in mice. *Circ Res*. 2005;97(4):372–379.

32. Pol CJ, Lieu M, Drosatos K. PPARs: Protectors or Opponents of Myocardial Function? *PPAR Res*. 2015;2015:835985.

33. Son NH, et al. PPARγ-induced cardiolipotoxicity in mice is ameliorated by PPARα deficiency despite increases in fatty acid oxidation. *J Clin Invest*. 2010;120(10):3443–3454.

34. Sena S, et al. Cardiac hypertrophy caused by peroxisome proliferator- activated receptor-gamma agonist treatment occurs independently of changes in myocardial insulin signaling. *Endocrinology*. 2007;148(12):6047–6053.

35. Chang CS, et al. Diuretics prevent thiazolidinedione-induced cardiac hypertrophy without compromising insulin-sensitizing effects in mice. *Am J Pathol*. 2014;184(2):442–453.

36. Son NH, et al. Cardiomyocyte expression of PPARgamma leads to cardiac dysfunction in mice. *J Clin Invest*. 2007;117(10):2791–2801.

37. Guan Y, et al. Thiazolidinediones expand body fluid volume through PPARgamma stimulation of ENaC-mediated renal salt absorption. *Nat Med*. 2005;11(8):861–866.

38. Zhang H, Zhang A, Kohan DE, Nelson RD, Gonzalez FJ, Yang T. Collecting duct-specific deletion of peroxisome proliferator-activated receptor gamma blocks thiazolidinedione-induced fluid retention. *Proc Natl Acad Sci USA*. 2005;102(26):9406–9411.

39. Dai C, Gu W. p53 post-translational modification: deregulated in tumorigenesis. *Trends Mol Med*. 2010;16(11):528–536.

40. Chang HC, Guarente L. SIRT1 and other sirtuins in metabolism. *Trends Endocrinol Metab*. 2014;25(3):138–145.

41. Lu M, et al. Brain PPAR-γ promotes obesity and is required for the insulin-sensitizing effect of thiazolidinediones. *Nat Med*. 2011;17(5):618–622.

42. Ryan KK, Li B, Grayson BE, Matter EK, Woods SC, Seeley RJ. A role for central nervous system PPAR-γ in the regulation of energy balance. *Nat Med*. 2011;17(5):623–626.

43. Ueki S, et al. Expression of PPARgamma in eosinophils and its functional role in survival and chemotaxis. *Immunol Lett*. 2003;86(2):183–189.

44. Qiu Y, et al. Eosinophils and type 2 cytokine signaling in macrophages orchestrate development of functional beige fat. *Cell*. 2014;157(6):1292–1308.

45. Wan Y, Chong LW, Evans RM. PPAR-gamma regulates osteoclastogenesis in mice. *Nat Med*. 2007;13(12):1496–1503.

46. Yamauchi T, et al. The mechanisms by which both heterozygous peroxisome proliferator-activated receptor gamma (PPARgamma) deficiency and PPARgamma agonist improve insulin resistance. *J Biol Chem*. 2001;276(44):41245–41254.

47. Miles PD, Barak Y, He W, Evans RM, Olefsky JM. Improved insulin-sensitivity in mice heterozygous for PPAR-gamma deficiency. *J Clin Invest*. 2000;105(3):287–292.

48. Rieusset J, et al. A new selective peroxisome proliferator-activated receptor gamma antagonist with antiobesity and antidiabetic activity. *Mol Endocrinol*. 2002;16(11):2628–2644.

49. Kubota N, et al. PPAR gamma mediates high-fat diet-induced adipocyte hypertrophy and insulin resistance. *Mol Cell*. 1999;4(4):597–609.

50. Heikkinen S, et al. The Pro12Ala PPARgamma2 variant determines metabolism at the gene-environment interface. *Cell Metab*. 2009;9(1):88–98.

51. Qiang L, Lin HV, Kim-Muller JY, Welch CL, Gu W, Accili D. Proatherogenic abnormalities of lipid metabolism in SirT1 transgenic mice are mediated through Creb deacetylation. *Cell Metab*. 2011;14(6):758–767.

52. Rosen ED, et al. C/EBPalpha induces adipogenesis through PPARgamma: a unified pathway. *Genes Dev*. 2002;16(1):22–26.

53. Cipolletta D, Cohen P, Spiegelman BM, Benoist C, Mathis D. Appearance and disappearance of the mRNA signature characteristic of Treg cells in visceral adipose tissue: age, diet, and PPARγ effects. *Proc Natl Acad Sci U S A*. 2015;112(2):482–487.